*materials*

MDPI

*Article*

# Evolution of the Microstructure and Phase Composition of the Products Formed in the Reaction between Iridium and $W_2B$

**Denis A. Bannykh [1], Victor V. Lozanov [1], Tatyana A. Gavrilova [2], Anatoly I. Beskrovny [3] and Natalya I. Baklanova [1,*]**

[1] Institute of Solid State Chemistry and Mechanochemistry SB RAS, 18 Kutateladze Str., Novosibirsk 630090, Russia
[2] Rzhanov Institute of Semiconductor Physics SB RAS, 13 Lavrentiev Ave., Novosibirsk 630090, Russia
[3] Joint Institute for Nuclear Research, 6 Joliot-Curie Str., Dubna 141980, Russia
* Correspondence: baklanova@solid.nsc.ru

**Abstract:** In the present study, we perform a systematic examination of the products formed by mixing and heating of tungsten boride and iridium powders at different ratios in a broad temperature range using qualitative and quantitative X-ray analysis and time-of-flight neutron diffraction (TOF-ND), in combination with scanning electron microscopy/energy-dispersive spectroscopy (SEM/EDS) performed at different accelerating voltages. The well-known and unknown ternary W–Ir–B phases were detected. The Vickers microhardness value for the new ternary $W_2Ir_5B_2$ boride was measured. Based on these findings, the ternary $W_2Ir_5B_2$ boride can be considered hard.

**Keywords:** tungsten; iridium; ternary boride; microhardness; intermetallics; microstructure



**Citation:** Bannykh, D.A.; Lozanov, V.V.; Gavrilova, T.A.; Beskrovny, A.I.; Baklanova, N.I. Evolution of the Microstructure and Phase Composition of the Products Formed in the Reaction between Iridium and $W_2B$. *Materials* **2022**, *15*, 7522. https://doi.org/10.3390/ma15217522

Academic Editors: Hansang Kwon and Irina Hussainova

Received: 20 September 2022
Accepted: 24 October 2022
Published: 26 October 2022



## 1. Introduction

Tungsten–iridium- and tungsten–iridium–boron-based materials are commonly demanded in the industry. These materials can be used for fabricating engines, cutting tools, wear-resistant and antioxidant coatings, as well as electrocatalysts due to the outstanding properties of both metals, including high melting points (2447 °C for Ir and 3422 °C for W), high level of mechanical properties, high hardness, and good oxidation resistance [1–11]. There are numerous examples where the synergistic effect of both metals significantly improved the properties of designed materials. Thus, the addition of iridium to tungsten increased the yield strength of the W–Ir alloy by 75% at 1727 °C [12] and the ductility of tungsten at room temperature [13]. Therefore, iridium can be considered a real alternative to rhenium, which was previously used in superalloys [12,13]. Good oxidation- and ablation-resistant W–Ir coatings for carbon supports were developed and successfully tested at high temperatures in an oxidative atmosphere [1,2]. Another positive example of the synergistic effect of both metals is the development of low-temperature brazing alloys for joining tungsten for high-temperature service [14]. The iridium–boron alloy systems with various proportions of tungsten have been used for this purpose. The addition of tungsten to the Ir–B alloy was found to increase the remelt temperature for joining. The remelt temperature for joining of tungsten varies in the range of 1800–2120 °C depending on the alloy composition. It suggests that the ternary W–Ir–B compounds with high melting points could be formed during joining.

The active expansion of the W–Ir and especially the W–Ir–B-based materials to new application areas is impeded by the fact that the available data on their composition, structure, and properties are scarce and contradictory. Several intermetallic compounds are known to exist in the Ir–W system, including $W_3Ir$ (P $4_2/mnm$), $W_xIr_{1-x}$ solid solution with a very wide homogeneity range (from 23–25 at.% to 52–57 at.% W) (P $6_3/mmc$), as well as two ordered WIr (P mma) and $WIr_3$ (P $6_3/mmc$) phases, each of them also having a homogeneity range of ~2 at.% W and 6 at.% W, respectively [15–21]. Both ordered phases

are displayed within the homogeneity region of $W_xIr_{1-x}$ solid solution. This might cause significant difficulties for interpreting the research results.

According to phase equilibria in the W–Ir–B system, there are only two ternary $W_2Ir_3B_{6-x}$ ($x \approx 1$) [22] and $W_{18}Ir_{13}B_{69}$ phases [23,24] in the boron-rich portion of the W–Ir–B system. In the metal-rich portion, the rapidly solidified W–Ir–B alloy (the 60:20:20 atomic ratio) was found to be composed of two crystalline phases (namely, the orthorhombic IrW and tetragonal $W_2B$ phases); no ternary borides were found [3]. Nevertheless, taking into account the high diversity of ternary borides for similar systems (Mo–Ir–B [22,25,26], Hf–Ir–B [27–30], and Zr–Ir–B [28,31]), one can suggest that ternary borides other than the aforementioned one could be formed in the W–Ir–B system. Here, it should be emphasized that the simultaneous presence of very heavy (W, Ir) and very light (B) elements in the composition is the main difficulty in investigating such a system.

In the present study, we performed a systematic examination of the products formed by mixing and heating of tungsten boride and iridium powders at different ratios in a broad temperature range using qualitative and quantitative X-ray analysis and time-of-flight neutron diffraction (TOF-ND), in combination with scanning electron microscopy/energy-dispersive spectroscopy (SEM/EDS) performed at different accelerating voltages. The well-known and unknown ternary W–Ir–B phases were detected. The Vickers microhardness value for the new ternary $W_2Ir_5B_2$ boride was measured. Based on these findings, ternary $W_2Ir_5B_2$ boride can be considered hard. Our findings expand the class of hard materials.

## 2. Materials and Methods

### *2.1. Initial Substances*

Iridium powder (purity $\geq$ 99.96%, GOST standard 12338–81, Krasnoyarsk, Russia) with the particle size D50 ~22 μm (Microsizer 201A analyzer) was mechanically pre-treated in a PM 100 CM planetary ball mill (Retsch, Haan, Germany) according to the procedure described by Bannykh et al. [32]. The lining of vials and the grinding media were made of WC. The particle size composition of powders was measured using a Microsizer 201 particle analyzer (Russian Federation State Standard GOST 57923-2017). The particle size of the mechanically treated iridium powder was equal to $D_{50}$~7.4 μm, $D_{90}$ = 15 μm. The habitus of particles was plate-like with a thickness of 100–300 nm. According to the EDS analysis, the iridium powder contained tungsten as a contaminant (~0.5 wt.%), which can be explained by the use of lining and grinding media composed of tungsten carbide.

The initial tungsten boride (Ltd. "Yumax", Ufa, Russia) contained 16 wt.% of the WB phase in addition to the dominant $W_2B$ phase. The initial tungsten boride was mechanically treated in a planetary ball mill. The particle size was found to be equal to $D_{50} \approx 400$ nm. After mechanical treatment, WC (1–2 wt.%) was detected as a contaminant. The cell parameters (a = 5.569 Å, c = 4.744 Å) and cell volume (V = 147.0 $Å^3$) of the $W_2B$ phase were in good agreement with the reference data (ICSD 42528) reported by Havinga et al. [33] and slightly lower than those reported by Kiessling [34,35]. This fact confirms the near-stoichiometric composition of $W_2B$. Contrariwise, the cell volume of the WB phase was estimated to be 162.4 $Å^3$, which corresponds to the composition of $WB_{0.96}$ [34].

### *2.2. Preparing the W–Ir–B Products and Their Characterization*

The W–Ir–B-based materials were obtained by mixing tungsten boride and iridium powders at different ratios in an agate mortar followed by consolidation by uniaxial pressing (P = 5 MPa, 30 s) at ambient temperature. The molar ratios of tungsten boride and iridium powder are listed in Table 1.

**Table 1.** The molar ratios of tungsten boride and iridium powder.

| Mixture | $W_2B$ (mol.%) | WB (mol.%) | Ir (mol.%) | Ir:W:B Molar Ratio |
|---|---|---|---|---|
| 1:1 | 26.9 | 9.6 | 63.5 | 1:1:0.6 |
| 3:1 | 11.9 | 4.2 | 83.9 | 3:1:0.6 |

Next, the pressed powder mixtures were loaded into grafoil boxes and placed into a high-temperature SNVE 1,7.3.1,7/20 vacuum furnace (Prizma, Iskitim, Russia), evacuated to P~$1.33 \cdot 10^{-3}$ Pa, heated to a given temperature (1000–1600 °C, with an increment of 100 °C) at a rate of 640 °C/h, and exposed to the given temperature for 1 h. The samples were cooled down under continuous vacuuming at a rate of 300 °C/h (5 °C/min).

The phase composition was studied using a Bruker D8 Advance X-ray powder diffractometer (Bruker Corporation, Billerica, MA, USA) employing CuK$\alpha$ radiation in the $10^\circ \leq 2\Theta \leq 110^\circ$ range. The time-of-flight neutron diffraction (TOF-ND) patterns of the product obtained after heating the powdered 1:1 mixture (1600 °C, 4 h) were collected using a real-time diffractometer of the IBR-2 reactor (FLNP JINR, Dubna, Russia) [36]. The surface morphology and local elemental composition of the samples were analyzed by scanning electron microscopy coupled with energy dispersive spectroscopy at an accelerating voltage of 15 kV, 20 kV, and 6 kV. The experimental details of analytical techniques are presented in the Supplementary Materials.

In order to measure the microhardness of different phases, the powdered products were packed into epoxy resin and polished. Vickers microhardness measurements were performed using a DuraScan-50 hardness testing machine (EMCO-TEST, Kuchl, Austria) at a load of 0.245 N (25 gf) in accordance with the ASTM E384-17 standard test method. The dwell time was 10 s.

## 3. Results and Discussion

### *3.1. Characterization of the Products Obtained via the Reaction between Tungsten Boride and Iridium Powders in the 1000–1200 °C Temperature Range*

According to the phase equilibria in the binary Ir–B, W–B, and W–Ir systems, the lowest-melting eutectic was formed in the Ir–B system at 1248 °C [37]. Therefore, one can consider the reaction between iridium and tungsten boride in the 1000–1200 °C temperature range to be a solid-state reaction. The X-ray diffraction data for the heat-treated 1:1 mixtures at 1000–1200 °C are presented in Figure 1a. One can see that no additional peaks besides those belonging to the initial reagents were observed in the products obtained at 1000 °C. The first feature of the reaction between $W_2B$ and Ir is the emergence of the XRD peaks belonging to iridium boride, $IrB_{1.1}$, and $W_xIr_{1-x}$ intermetallics ($2\Theta = 57.05^\circ$) in the products obtained at 1100 °C. The composition of the intermetallic phase was calculated to be $W_{0.23}Ir_{0.77}$ in accordance with the Vegard's rule. For calculation, the reference data by Tylkina et al. [18] and Raub et al. [15] were used. The formation of these products probably occurred according to reaction 1. Here, x is 0.23.

$$11xW_2B + (22 - 12x)Ir \rightarrow 10xIrB_{1.1} + 22W_xIr_{1-x} \quad (1)$$

The phase composition of the products obtained at 1200 °C in the 1:1 mixtures was found to also be presented by WB and $W_xIr_{1-x}$. The quantitative X-ray analysis showed that the content of the WB phase was 27 wt.% (1200 °C), which is much higher than that in the initial reagent (see Supplementary Materials). The additional quantity of the WB phase could have arisen from the reaction between iridium and the $W_2B$ phase. The peak maxima of the WB phase shifted noticeably towards large angles. This is accompanied by an increase in the WB cell volume from 162.4 Å$^3$ to 163.4 Å$^3$. Taking into account the cell volume–composition relationship for $WB_{1-x}$ proposed by Kiessling [34], the phase composition of the $WB_{1-x}$ phase was calculated to change from $WB_{0.96}$ to $WB_{0.98}$. The other phase formed via the reaction between iridium and tungsten boride at 1200 °C; the $W_xIr_{1-x}$ substitutional solid solution (~73 wt.%) has a very broad homogeneous range, namely, x = 0.25–0.53.

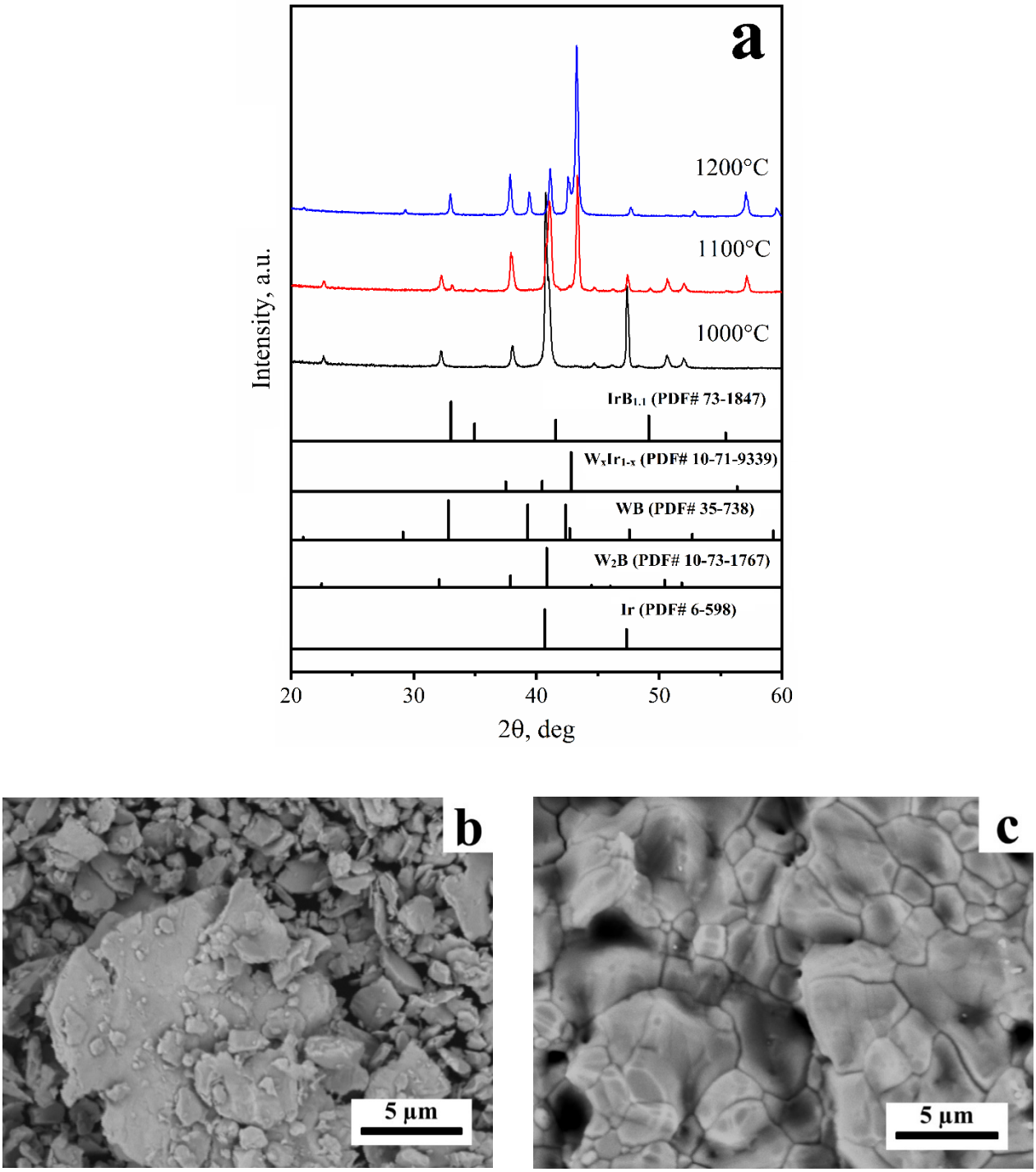


**Figure 1.** The XRD patterns (**a**) and SEM images ((**b**)—1100 °C, (**c**)—1200 °C) of the products obtained via the reaction between iridium and tungsten (1:1 mixture).

The behavior of the 3:1 mixture differs from that for the 1:1 mixture. After heat treatment at 1200 °C, the XRD peaks belonging not only to $W_{0.23}Ir_{0.77}$ (87 wt.%) and WB (4.5 wt.%), but also to $IrB_{1.1}$ are observed (Figure 2a). The formation of the aforementioned products can be attributed to Reaction (2):

$$xW_2B + (1 - x)Ir = xWB + W_xIr_{1-x} \quad (2)$$

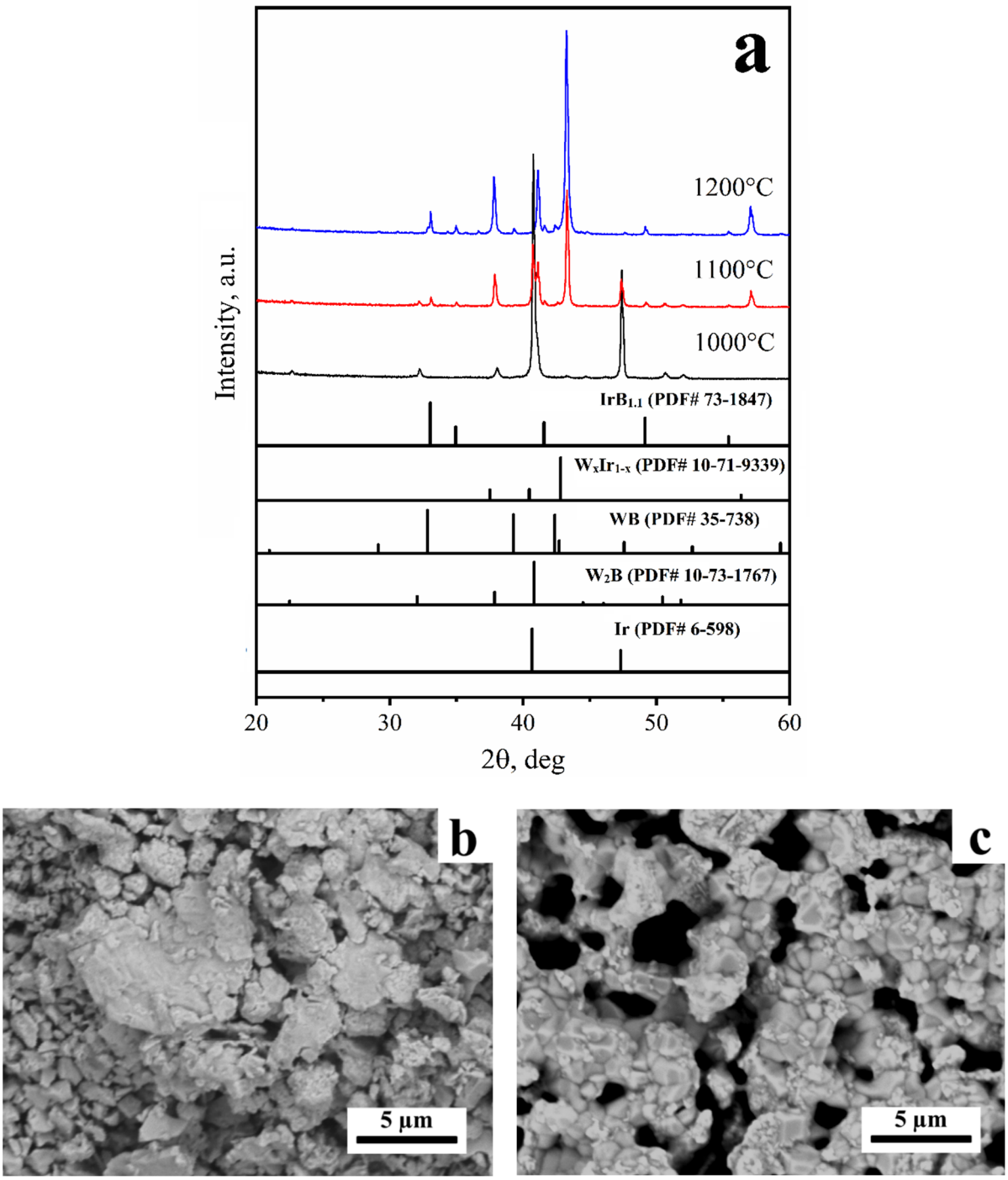


**Figure 2.** The XRD patterns (**a**) and SEM images ((**b**)—1100 °C, (**c**)—1200 °C) of the products obtained via the reaction between iridium and tungsten (3:1 mixture).

The morphology of the products obtained at 1200 °C was changed compared with that observed for the products at 1000 °C and 1100 °C; particles of irregular habitus were detected, being connected with each other by bridges (Figure 2b,c).

### *3.2. Characterization of the Products Obtained via the Reaction between Tungsten Boride and Iridium in the 1300–1600 °C Temperature Range*

#### 3.2.1. The 1:1 Mixtures

According to the XRD analysis, only the WB and $W_xIr_{1-x}$ phases are present in the products obtained in the 1300–1600 °C temperature range (reaction 2, Figure 3a).

Broad asymmetric peaks with a complex contour were detected in the XRD pattern of the product formed at 1300 °C. These peaks can be fairly well described by three components corresponding to the compositions $W_{0.25}Ir_{0.75}$, $W_{0.5}Ir_{0.5}$, and $W_{0.33}Ir_{0.67}$. The latter one is dominant in accordance with the quantitative XRD analysis (Figure 3b). According to the data reported in [20], the ordered $W_{0.25}Ir_{0.75}$ ($WIr_3$) and $W_{0.5}Ir_{0.5}$ (WIr) phases have crystal structure types $MgCd_3$ and AuCd, respectively. The XRD peaks of the $W_{0.25}Ir_{0.75}$ and $W_{0.5}Ir_{0.5}$ intermetallic phases disappear as the temperature increases (1400 °C and above). This result is not surprising because the $W_{0.33}Ir_{0.67}$ phase is thermodynamically the most stable [38].

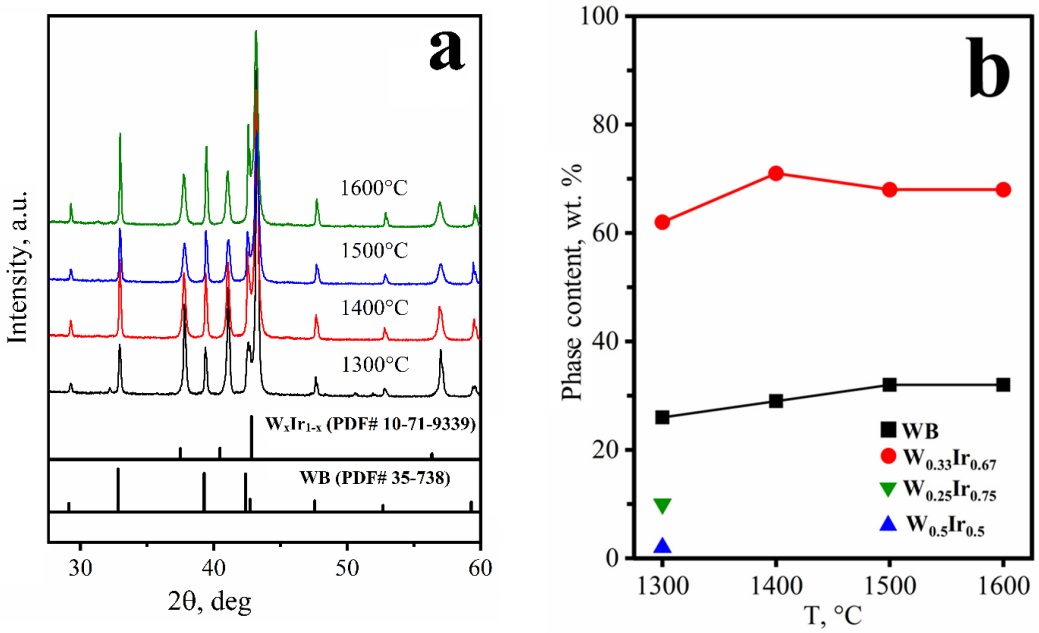


**Figure 3.** The XRD patterns (**a**) and phase composition (**b**) of the products depending on temperature.

As mentioned above, tungsten boride was also found among the products obtained in the 1300–1600 °C temperature range. As the temperature rises, the composition of $WB_x$ approaches $WB_{0.96}$ [39]; furthermore, the coherent-scattering region increases gradually, which can argue in favor of the growth of WB grains. The results of quantitative XRD analysis are presented in Figure 3b. One can see that the $W_xIr_{1-x}$:WB ratio is almost constant in the 1300–1600 °C temperature range.

Additional important information about the phase composition can be obtained from the TOF-ND analysis data (Figure 4). In addition to the peaks associated with the WB and $W_xIr_{1-x}$ solid solution, low-intensity peaks at d~3.25 and 2.80 Å can be seen in the TOF-ND patterns (Figure 4a). Each of the broad peaks at d~3.25 Å and 2.80 Å can be deconvoluted into two components (Figure 4b). The comparison of peak positions allows us to ascribe them to the ordered intermetallic WIr and $WIr_3$ phases [20]. The results of the quantitative TOF-ND analysis are summarized in Table 2. It follows from Table 2 that the intermetallic phase is made of ordered phases by 50%; the remaining part is the disordered $W_xIr_{1-x}$ solid solution. The cell volume of $WIr_3$ was 0.2% larger, and the cell volume of WIr was 0.8% smaller than those reported in the Springer Materials database. These results are in accordance with previously reported data about the homogeneity regions for the ordered intermetallic WIr and $WIr_3$ phases [21].

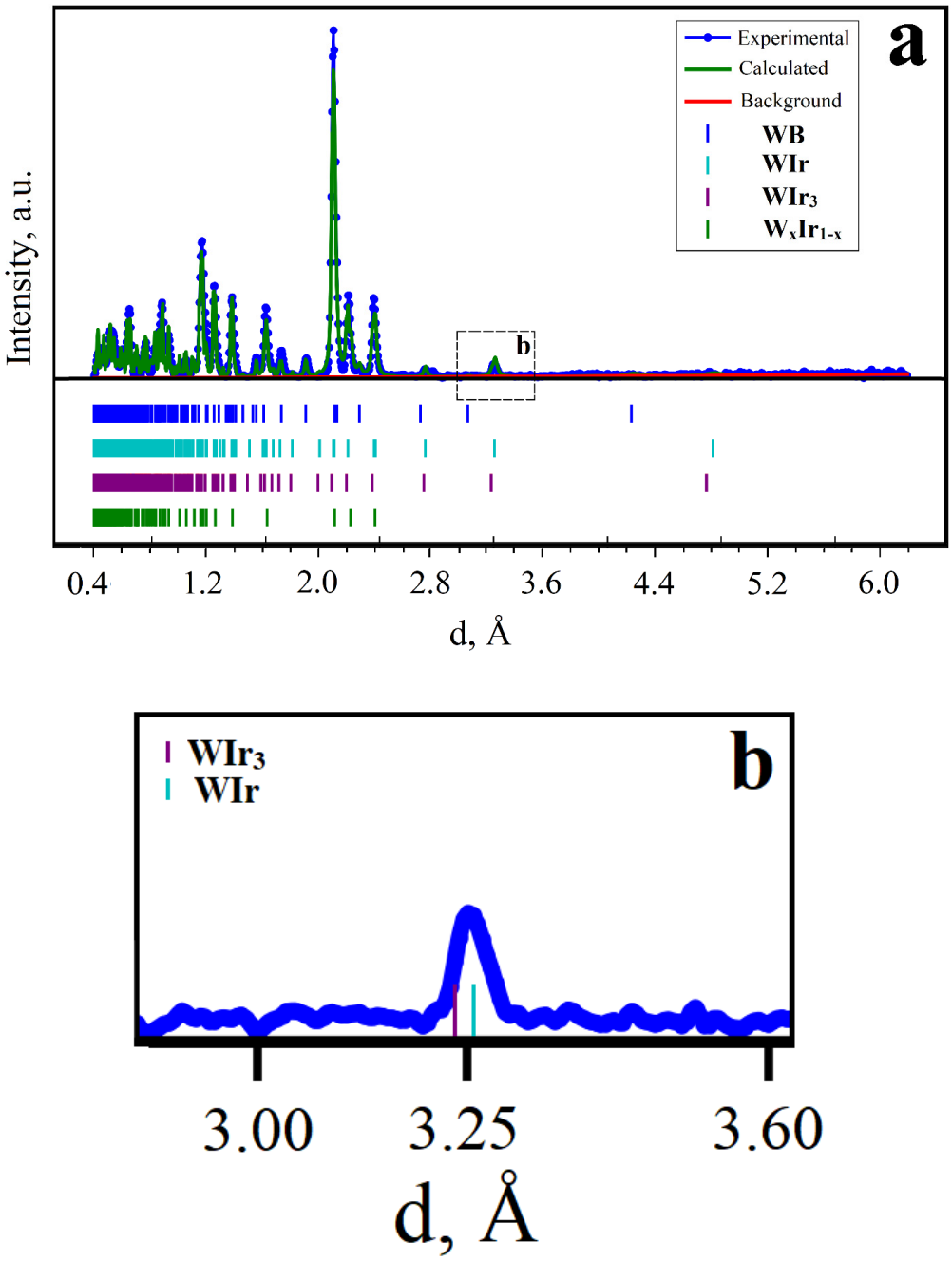


**Figure 4.** The TOF-ND pattern of the product obtained at 1600 °C, 4h (**a**). The TOF-ND superstructure peak for the ordered $WIr_3$ and WIr phases (**b**).

Hence, the TOF-ND method allowed us to clearly detect the formation of both ordered and disordered intermetallic W–Ir phases. We would like to note that it could not be achieved by X-ray analysis because of the coincidence of high-intensity X-ray peaks of the ordered and disordered intermetallic phases and the absence of superstructure peaks belonging to the ordered $WIr_3$ and WIr phases.

Unfortunately, it was impossible to prepare a section of the sample heat-treated at 1300 °C to study its microstructure because the sample was characterized by high porosity, causing particle chipping during sample preparation (Supplementary Materials, Figure S1). Figure 5a–c show the typical SEM images of the cross-section of the products obtained at higher temperatures. The SEM/EDS analysis demonstrated that the grains varied in contrast, thus indicating that spots with different elemental compositions were formed. In accordance with the EDS analysis data, dark gray grains belonged to WB. The linear size of WB particles was found

with the ImageJ software to be equal to 2–7 μm (T = 1400 °C), 5–17 μm (T = 1500 °C), and 6–20 μm (T = 1600 °C). As the temperature rose, the size of WB aggregates increased (70 μm, 100 μm, and 110 μm for 1400 °C, 1500 °C, and 1600 °C, respectively). The distinct contrast of an individual WB grain can be attributed to some deviation in composition and/or formation of a solid solution. WB aggregates are surrounded by the light gray $W_xIr_{1-x}$ phase whose composition is represented by $W_{0.33}Ir_{0.67}$ (predominantly) and $W_{0.25}Ir_{0.75}$ (Figure 5d, respectively). The porosity decreases with increasing temperature. In general, the microstructures of the products obtained at 1500 and 1600 °C are almost indistinguishable. The phase compositions for both temperatures also coincide.

**Table 2.** The quantitative and qualitative TOF-ND analysis data for the product obtained at 1600 °C for 4 h.

| Phase | Crystal Structure | Lattice Parameters, Å | Volume, Å$^3$ | Content, wt.% |
|---|---|---|---|---|
| WB | I $4_1$/amd | a = 3.113<br>c = 16.90 | 163.8 | 16 |
| $WIr_3$ | P $6_3$/mmc | a = 5.499<br>c = 4.394 | 115.07 | 19 |
| WIr | P mma | a = 4.417<br>b = 2.760<br>c = 4.808 | 58.62 | 23 |
| $W_xIr_{1-x}$ | P $6_3$/mmc | a = 2.771<br>c = 4.457 | 29.65 | 42 |

3.2.2. The 3:1 Mixtures

The results of qualitative X-ray analysis of the 3:1 mixtures heated at different temperatures showed that the products are composed of the $W_xIr_{1-x}$ (x ≈ 0.25), $IrB_{1.1}$, WB, and $W_2Ir_3B_{6-x}$ phases (Figure 6). The presence of the $IrB_{1.1}$ phase in the product suggests that reactions involving liquids occur in the 1300–1600 °C temperature range. Another interesting feature is the emergence of XRD peaks belonging to the ternary $W_2Ir_3B_{6-x}$ boride phase. According to the phase equilibrium in the W–Ir–B system, the $W_2Ir_3B_{6-x}$ phase is a single ternary boride. Finally, the most important observation is the presence of a series of XRD peaks that cannot be ascribed to any known binary or ternary phases in the W–Ir–B system. These peaks are listed in Table S1 of the Supplementary Materials.

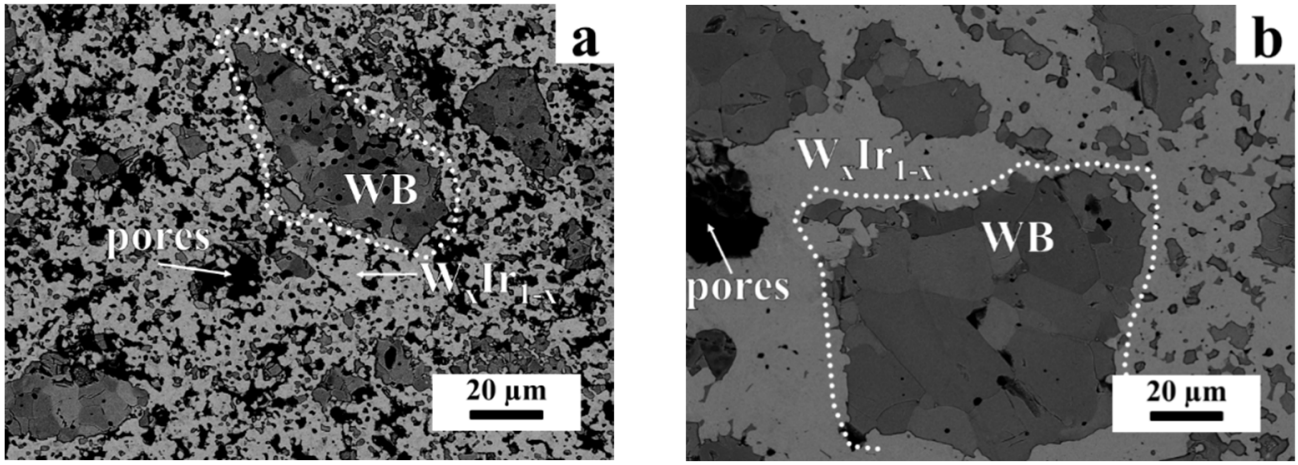


**Figure 5.** *Cont.*

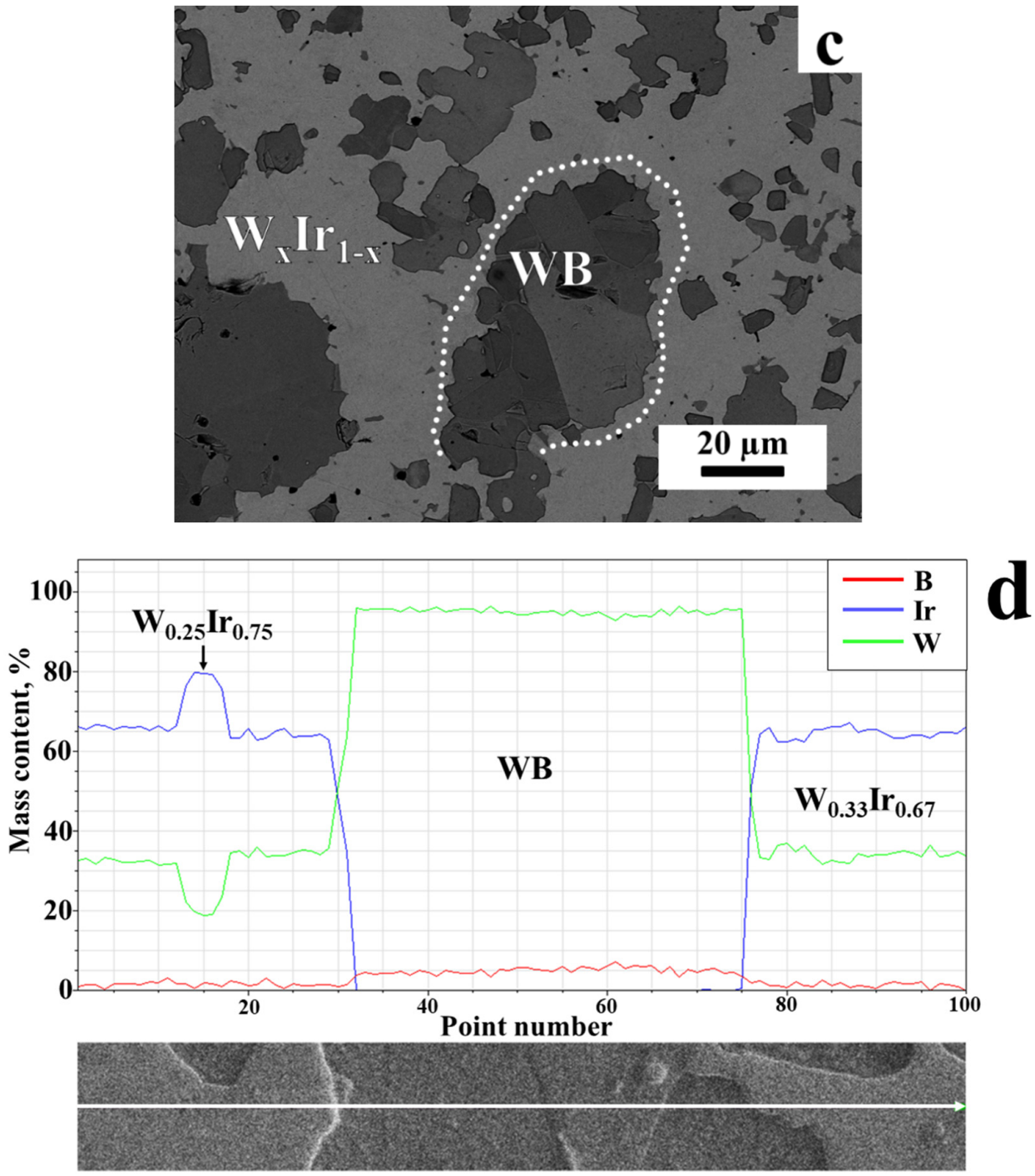


**Figure 5.** SEM images of the cross sections of the mixtures heat-treated at different temperatures: (**a**) 1400 °C; (**b**) 1500 °C; and (**c**) 1600 °C (accelerating voltage, 20 kV). (**d**)—The EDS analysis data (accelerating voltage, 6 kV) of the cross section of the product obtained at 1600 °C. Element distribution along the white arrow is shown.

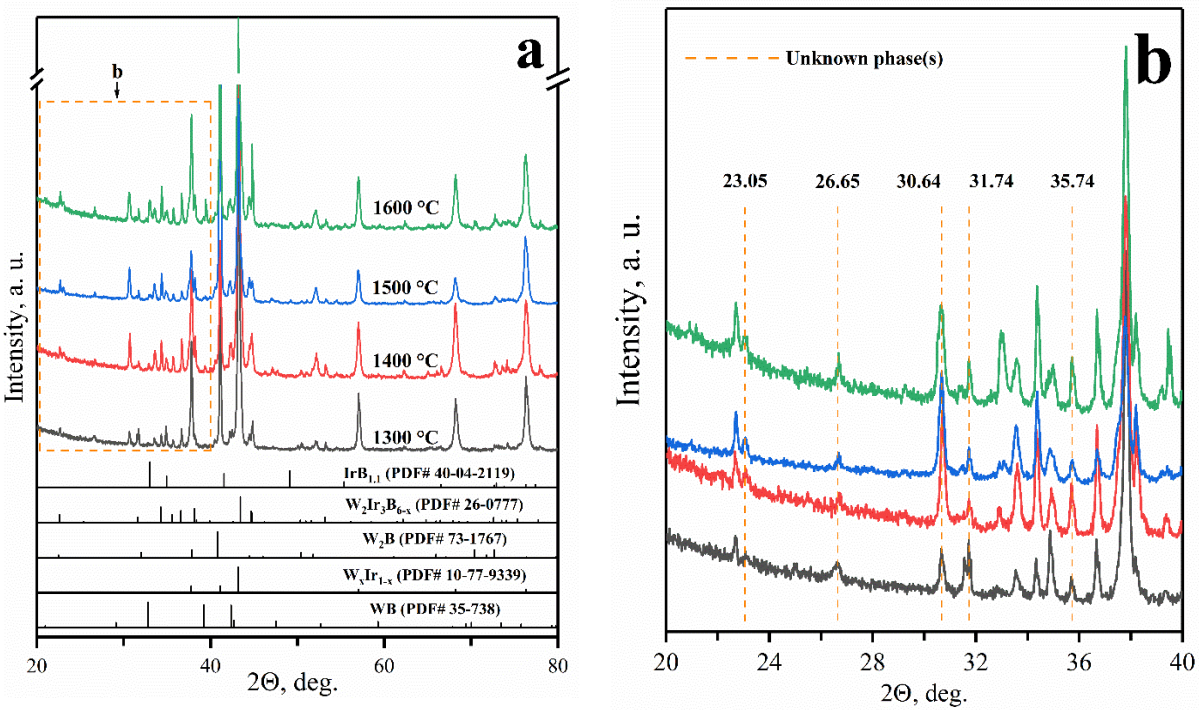


**Figure 6.** The XRD patterns of the Ir:$W_2B$ = 3:1 mixtures heat treated in the temperature range of 1300–1600 °C (**a**). Inset (**b**): the XRD peaks of an unknown phase(s).

It follows from the TOF-ND pattern that the peaks belonging to $IrB_{1.1}$, the intermetallic $W_xIr_{1-x}$ solid solution, as well as the ordered $WIr_3$ phase, have emerged. In addition, the non-identified peaks in the $d$ = 0.4–1.0 Å range were detected. They can probably be related to the formation of an unknown ternary boride phase(s) (Supplementary Materials, Figure S2).

The BSE SEM/EDS images of two typical cross sections of the products obtained in the 3:1 mixtures are shown in Figure 7a,b (accelerating voltage of 20 kV). One can observe several types of areas distinct in color that indicate different elemental compositions. The dark gray areas were ascribed to $IrB_{1.1}$. The EDS spectra were processed in terms of the W/Ir atomic ratio. Surprisingly, for both the light gray and middle gray large areas that clearly differ in contrast, the W:Ir ratio was almost similar and close to 0.27–0.28:0.73–0.72. This can imply that the contrast differed in these areas because of the presence of a third element (e.g., boron) in the middle gray areas. Indeed, a hardly noticeable shoulder with a maximum at ~180–200 eV is observed in the EDS spectrum taken from the middle gray area at an accelerating voltage of 20 kV (Figure 7c). One can note that the maximum coincides with the B-K line [40,41] and overlapped with the W-N (208, 212.2, 222.1, 229.5 eV) and Ir-N (234.8, 247 eV) lines [42]. In this special case, the M lines of tungsten and iridium are usually used to determine the elemental composition. As seen from Figure 7d, no shoulder was present in the EDS spectrum taken from the light gray area. It suggests that this area belongs to the boron-free phase.

The EDS analysis performed at an accelerating voltage of 6 kV allowed us to determine the elemental composition more comprehensively (including detecting boron) (Figure 8). Elemental mapping of random grains shows that different phases are present. Together with the intermetallic $W_{0.25}Ir_{0.75}$ phase, another intermetallic phase, $W_xIr_{1-x}$ ($x \approx 0.33$), was also detected; however, it was a very rare occurrence (Supplementary Materials, Figures S3 and S4). In addition, the WB and $IrB_{1.1}$ phases were also found. The most interesting fact is the presence of two types of middle gray areas simultaneously containing tungsten, iridium, and boron at different ratios. The EDX spectra of the selected areas are shown in Figure 8e,f. One of them had the $W_2Ir_3B_{6-x}$ composition, where x = 0.35–0.87; the other one had a statistical composition $W_{2.2\pm0.1}Ir_5B_{2.3\pm0.2}$ (Figure 8e). It is worth noting that the latter phase has never been previously reported for the W–Ir–B system. All the experimental EDS

analysis data for new ternary phase in the present study were processed as the dependence of the B/(W + Ir) ratio on the Ir/(W + Ir) ratio (Figure 9). One should bear in mind that each detected ternary phase under consideration varies insignificantly in heavy metal contents, but can significantly vary in boron content. Thus, taking into account the EDS and XRD data, the $W_2Ir_5B_2$ phase can be considered as a new ternary boride.

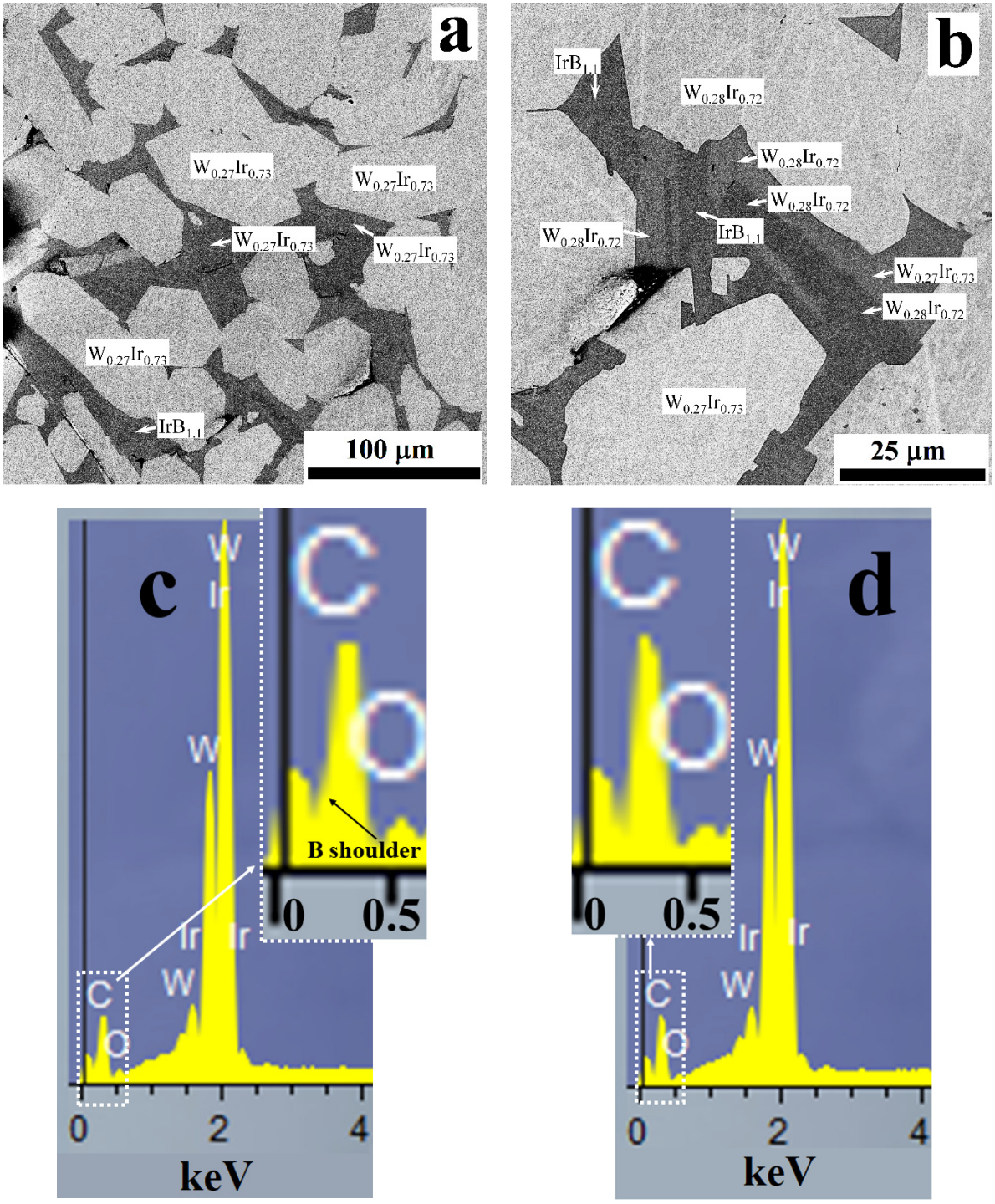


**Figure 7.** The BSE SEM/EDS images of two typical cross sections of the products obtained in the 3:1 mixtures (**a**,**b**). The EDS spectra taken from the selected areas: (**c**)—middle gray area belonging to the boron-containing phase; (**d**)—light gray area belonging to boron-free phase.

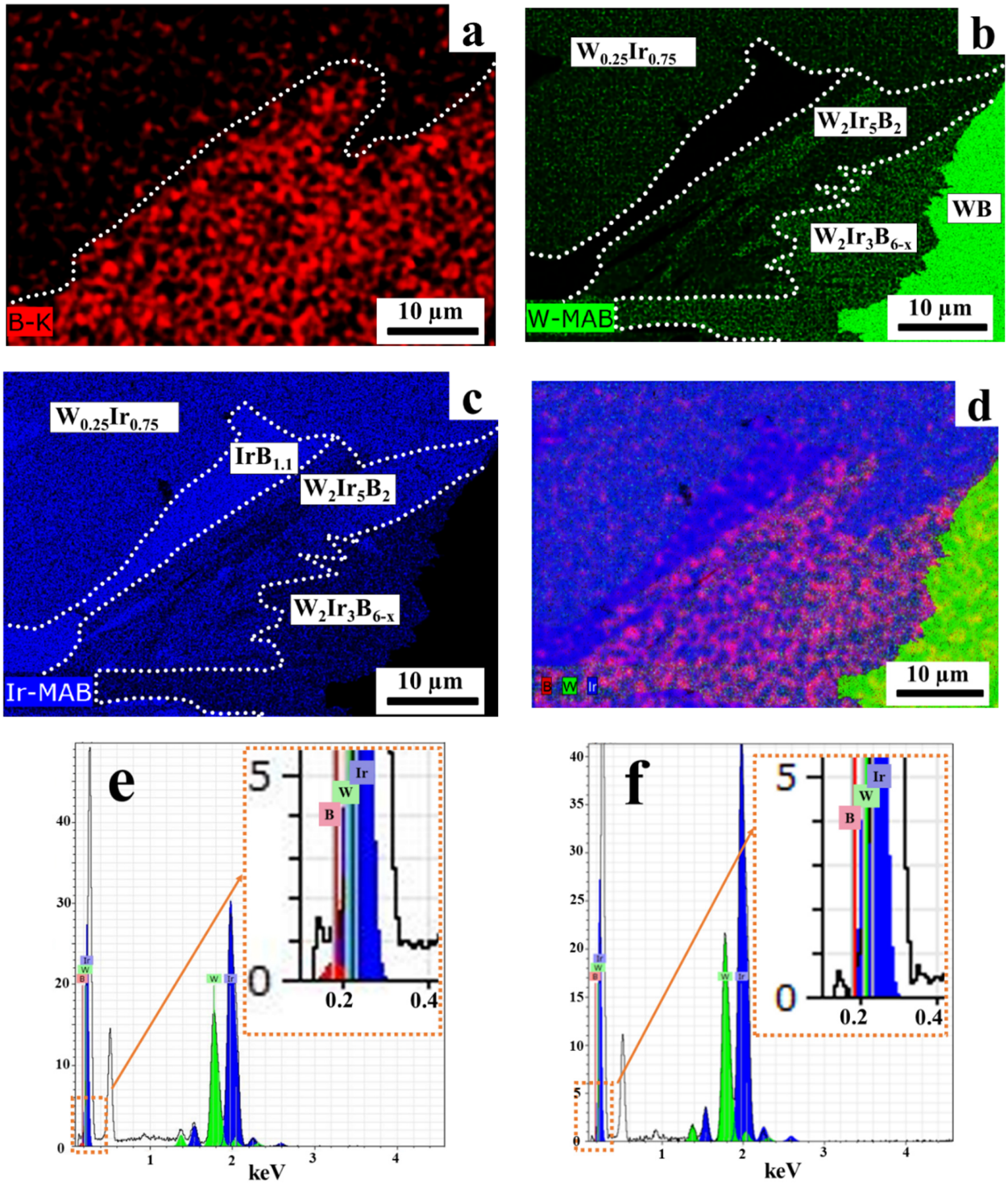


**Figure 8.** (**a**–**f**) The EDS spectra (accelerating voltage, 6 kV) of the cross sections of the products obtained at 1600 °C; (**a**–**c**) elemental mapping of random grains demonstrating the formation of different phases. Here, B, Ir, and W are colored by red, blue, and green, respectively; (**d**) cameo BS SEM/EDS image. The EDX spectra of the selected areas: $W_2Ir_5B_2$ (**e**) and $W_{0.25}Ir_{0.75}$ (**f**) phases.

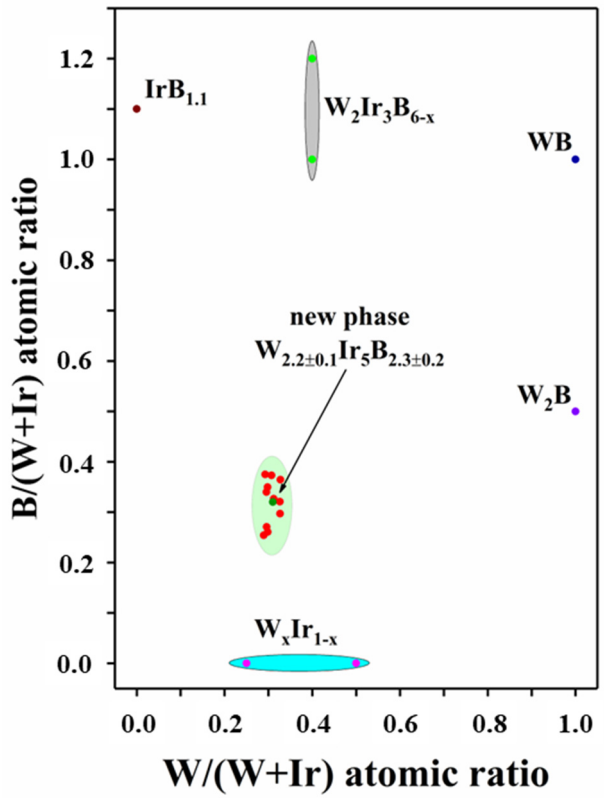


**Figure 9.** The B/(W + Ir) ratio as a function of the Ir/(W + Ir) ratio. The findings for the known phases of the binary W–Ir, B–Ir, W–B, and ternary W–Ir–B systems are also shown. Red points are the energy-dispersive X-ray spectrometry (EDS) data for $W_2Ir_5B_2$; the reference data for the known compounds are as follows: wine-colored points—$IrB_{1.1}$; royal blue points—WB; violet points—$W_2B$; magenta points—$W_xIr_{1-x}$; and green points—$W_2Ir_3B_{6-x}$.

Thus, the data on phase and elemental compositions of the products formed by heat treatment of the 3:1 mixtures were obtained. The good reproducibility of the powder XRD, SEM/EDS, and TOF-ND analysis data unambiguously confirms that a novel ternary boride with tentative composition $W_2Ir_5B_2$ is formed at temperatures higher than 1300 °C. No phase with a similar composition has been previously reported for the W–Ir–B system. In our opinion, a key factor contributing to the formation of ternary boride phases via the reaction between iridium and tungsten boride is the emergence of liquid iridium boride at temperatures above 1300 °C. This is a liquid phase, which promotes improved mass transfer and ensures the formation of ternary borides, $W_2Ir_3B_6$ and $W_2Ir_5B_2$.

### *3.3. Microhardness*

In this work, the Vickers microhardness values for binary intermetallic areas and new ternary $W_2Ir_5B_2$ boride were measured at a load of 0.245 N. The results are presented in Figure 10. The mean microhardness of intermetallic areas (without boron) with composition $W_{0.36}Ir_{0.64}$ is ~13.1 ± 2.0 GPa (18 tests), whereas the microhardness of hexagonal $WIr_3$ crystals was evaluated to be 10.7 ± 1.6 GPa (104 tests). These microhardness values are in good agreement with the data previously reported by Tylkina et al. for similar compositions [18] and are somewhat lower than those reported by E. Raub et al. [15] (Table 3). The microhardness value for the new ternary boride, $W_2Ir_5B_2$, was measured for the first time and was equal to 15.5 ± 3.1 GPa (16 tests). Based on this result, the new ternary boride can be considered the hard phase. This value is lower than that reported previously for the ternary Hf–Ir–B boride of similar composition (18.2 ± 1.7 GPa for $Hf_2Ir_5B_2$) [30].

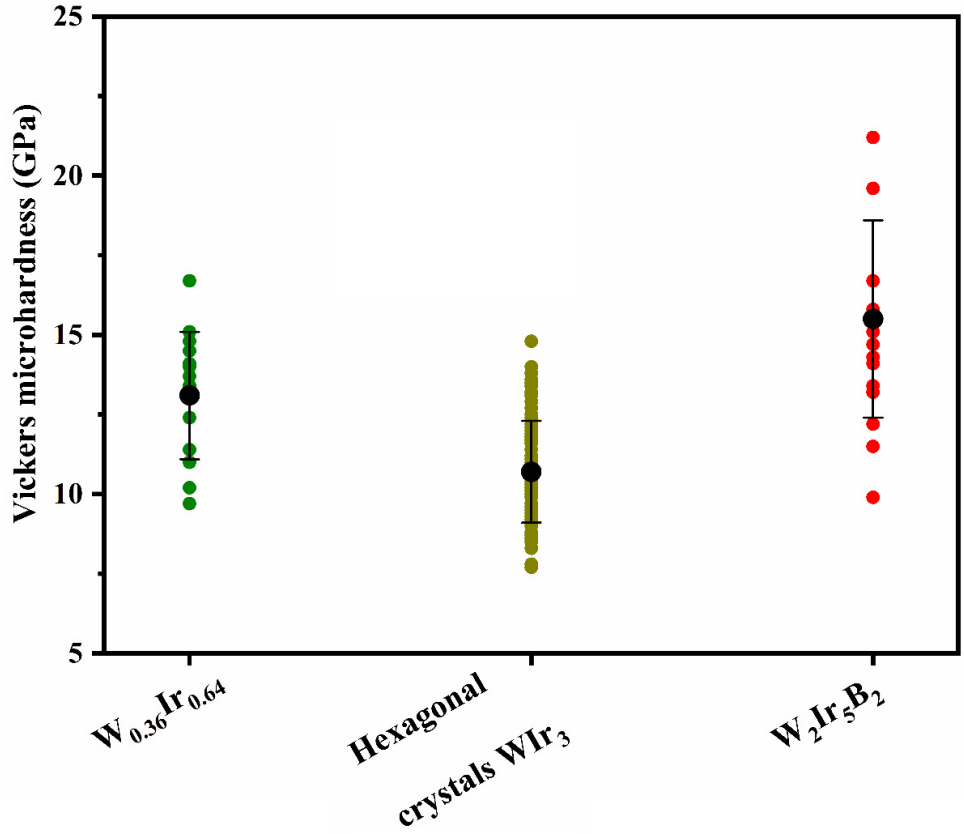


**Figure 10.** Microhardness of intermetallic areas and the new ternary $W_2Ir_5B_2$ phase in the products obtained at 1600 °C, 4 h.

**Table 3.** Comparison of the mean Vickers microhardness values (load, 0.245 N) for different intermetallic W–Ir phases studied in this work to those reported previously.

| Reference | Microhardness, GPa | |
|---|---|---|
| | W, ~26 at.% | W, ~36 at.% |
| This study | 10.7 ± 1.6 | 13.1 ± 2.0 |
| Tylkina et al. [18] | 10.8 | 12.7 |
| Raub et al. [15] | 13.2 * | 15.2 ** |

* 24 at.% W; ** 34 at.% W.

## 4. Conclusions

The products of the reaction between iridium and tungsten diboride were studied in a broad temperature range (1000–1600SC) using X-ray powder diffraction analysis and SEM/EDS at different accelerating voltages, and TOF-ND analysis. It was stated that the phase composition of the products varies depending on the experimental conditions and can include the intermetallic $W_xIr_{1-x}$ phases, $IrB_{1.1}$, and ternary W–Ir–B borides. A set of analytical techniques unambiguously confirmed that the novel ternary boride with statistical composition $W_{2.2\pm0.1}Ir_5B_{2.3\pm0.2}$ was formed together with the known $W_2Ir_3B_{6-x}$ ternary boride at temperatures above 1300 °C. No phase with a similar composition ($W_2Ir_5B_2$) has been previously reported for the W–Ir–B system. It was suggested that emergence of liquid iridium boride at temperatures above 1300 °C improves mass transfer and contributes to the formation of a variety of ternary borides, $W_2Ir_3B_6$ and $W_2Ir_5B_2$. The Vickers microhardness values for new ternary $W_2Ir_5B_2$ boride were measured at a load of 0.245 N. The microhardness was found to be equal to 15.5 ± 3.1 GPa. Based on these findings, the new ternary boride can be considered a hard phase.

Due to compositional diversity, the phases formed via the reaction between tungsten boride and iridium can have a broad range of physical and chemical properties. This fact offers additional opportunities for designing structural materials with improved properties for high-temperature applications.

**Supplementary Materials:** The following supporting information can be downloaded at: https://www.mdpi.com/article/10.3390/ma15217522/s1, Figure S1: SEM image of the sample heat-treated at 1300 °C after preparation of cross-section; Figure S2: The TOF-ND of the products obtained in the 3:1 mixture at 1600 °C. The *d* range in which the unidentified peaks were detected is denoted by dashed line; Figure S3: The BSE SEM/EDS image and elemental composition of the area belonging to the $W_xIr_{1-x}$ intermetallic phase (where $x \approx 0.33$); Figure S4. The BSE SEM/EDS image and elemental composition of the area belonging to the $W_xIr_{1-x}$ intermetallic phase (where $x \approx 0.33$); Table S1: The unidentified *d* spacing and the corresponding 2Θ. Reference [43] are cited in the supplementary materials.

**Author Contributions:** Conceptualization, N.I.B.; Investigation, D.A.B., V.V.L., T.A.G. and A.I.B.; Writing—original draft, V.V.L. All authors have read and agreed to the published version of the manuscript.

**Funding:** This research was funded by the Russian Science Foundation (grant number 18-19-00075).

**Institutional Review Board Statement:** Not applicable.

**Informed Consent Statement:** Not applicable.

**Data Availability Statement:** The data presented in this study are available on request from the corresponding author.

**Acknowledgments:** The authors are grateful to A. Ukhina for the XRD measurements.

**Conflicts of Interest:** The authors declare no conflict of interest.

## References

1. Wu, W.; Chen, Z.; Cheng, H.; Wang, L.; Zhang, Y. Tungsten and iridium multilayered structure by DGP as ablation-resistance coatings for graphite. *Appl. Surf. Sci.* **2011**, *257*, 7295–7304. [CrossRef]
2. Chen, Z.; Tao, J.; Xu, Z. Tungsten/Iridium Composite Coating Layer for Carbon Material Antioxidation and Its Preparation Method. Patent CN1904127A, 12 November 2008.
3. Li, R.; Wang, H.; Hu, F.; Chan, K.C.; Liu, X.; Lu, Z.; Wang, J.; Li, Z.; Zeng, L.; Li, Y.; et al. IrW nanochannel support enabling ultrastable electrocatalytic oxygen evolution at 2 A $cm^{-2}$ in acidic media. *Nat. Commun.* **2021**, *12*, 3540. [CrossRef]
4. Lv, F.; Feng, J.; Wang, K.; Dou, Z.; Zhang, W.; Zhou, J.; Yang, C.; Luo, M.; Yang, Y.; Li, Y.; et al. Iridium–Tungsten Alloy Nanodendrites as pH-Universal Water-Splitting Electrocatalysts. *ACS Central Sci.* **2018**, *4*, 1244–1252. [CrossRef] [PubMed]
5. Hill, V.L.; Malatesta, M.J. *Investigation of Refractory Composites for Liquid Rocket Engines*; IIT Research Institute: Chicago, IL, USA, 1970. Available online: https://ntrs.nasa.gov/archive/nasa/casi.ntrs.nasa.gov/19710019025.pdf (accessed on 6 August 2013).
6. Mościcki, T.; Chrzanowska-Giżyńska, J.; Psiuk, R.; Denis, P.; Mulewska, K.; Kurpaska, Ł.; Chmielewski, M.; Wiśniewska, M.; Garbiec, D. Thermal and mechanical properties of (W,Zr)B2-z coatings deposited by RF magnetron sputtering method. *Int. J. Refract. Met. Hard Mater.* **2022**, *105*, 105811. [CrossRef]
7. Navarrete-Cuadrado, J.; Soria-Biurrun, T.; Lozada-Cabezas, L.; Moseley, S.; Alveen, P.; Gonzalez-Polvorosa, N.; Tarragó, J.M.; Sanchez-Moreno, J.M. Hot isostatic pressing of $WB_4$ and $WB_4$-$TaB_2$ based ultrahard materials. *Int. J. Refract. Met. Hard Mater.* **2022**, *109*, 105965. [CrossRef]
8. Cruz, L.; Jacobson, D. Sub-surface iridium depletion in dilute solution tungsten-iridium alloys due to high temperature work function testing. *Int. J. Refract. Met. Hard Mater.* **1992**, *11*, 223–234. [CrossRef]
9. Ohriner, E.; Zhang, W.; Ulrich, G. Analysis of abrasive blasting of DOP-26 iridium alloy. *Int. J. Refract. Met. Hard Mater.* **2012**, *35*, 122–126. [CrossRef]
10. Kvashnin, A.G.; Zakaryan, H.A.; Zhao, C.; Duan, Y.; Kvashnina, Y.A.; Xie, C.; Dong, H.; Oganov, A.R. Oganov, New tungsten borides, their stability and outstanding mechanical properties. *J. Phys. Chem. Lett.* **2018**, *9*, 3470–3477. [CrossRef]
11. Kvashnin, A.G.; Samtsevich, A.I. Phase Transitions in Tungsten Monoborides. *J. Exp. Theor. Phys. Lett.* **2020**, *111*, 343–349. [CrossRef]
12. Corti, C.W. Tungsten-iridium alloys at high temperatures. *Platin. Met. Rev.* **1992**, *36*, 13.
13. Luo, A.; Jacobson, D.; Shin, K. Solution softening mechanism of iridium and rhenium in tungsten at room temperature. *Int. J. Refract. Met. Hard Mater.* **1991**, *10*, 107–114. [CrossRef]
14. Pattee, H.E.; Evans, R.M. *Brazing and Bonding of Columbium, Molybdenum, Tantalum, Tungsten, and Graphite*; Defense Metals Information Center, Battelle Memorial Institute: Columbus, OH, USA, 1962. Available online: https://apps.dtic.mil/sti/pdfs/AD0278193.pdf (accessed on 7 March 2021).

15. Raub, E.; Walter, P. Die Legierungen der Platinbeimetalle mit Wolfram. In *Festschrift aus Anlass des 100-Jahrigen Jubilaums der Firma*; Ruthardt, K., Ed.; WC Heraeus GmbH: Hanau, Germany, 1951; pp. 124–146.
16. Knapton, A.G. An X-ray survey of certain transition-metal systems for sigma phases. *J. Inst. Met.* **1958**, *87*, 28–32.
17. Rapperport, E.J.; Smith, M.F. *Refractory Metal Constitution Diagrams*; Constitution Diagrams W-Rh, W-Ir; Nuclear Metals Inc.: Concord, MA, USA, 1962. Available online: https://apps.dtic.mil/sti/pdfs/AD0287548 (accessed on 7 March 2021).
18. Tylkina, M.A.; Polyakova, V.P.; Shekhtman, V.S. Sistema iridii—Volfram (Iridium—Tungsten system). *Zh. Neorg. Khim.* **1963**, *8*, 2549–2555. (In Russian)
19. Giessen, B.C.; Grant, N.J. New intermediate phases in transition metal systems, III. *Acta Crystallogr.* **1965**, *18*, 1080–1081. [CrossRef]
20. Giessen, B.; Jaehnigen, U.; Grant, N. Ordered AB and AB3 phases in T6-T9 alloy systems and a modified Mo-lr phase diagram. *J. Less Common Met.* **1966**, *10*, 147–150. [CrossRef]
21. Omori, T.; Makino, K.; Shinagawa, K.; Ohnuma, I.; Kainuma, R.; Ishida, K. Phase equilibria and mechanical properties of the Ir–W–Al system. *Intermetallics* **2014**, *55*, 154–161. [CrossRef]
22. Rogl, P.; Benesovsky, F.; Nowotny, H. Über einige Komplexboride mit Platinmetallen. *Monatshefte für Chemie* **1972**, *103*, 965–989. [CrossRef]
23. Rogl, P.; Nowotny, H.; Benesovsky, F. Ternäre Komplexboride in den Dreistoffen: {Mo, W}−{Ru, Os}−B und W−Ir−B. *Monatshefte für Chemie* **1970**, *101*, 850–854. [CrossRef]
24. Zeiringer, I.; Rogl, P.; Grytsiv, A.; Polt, J.; Bauer, E.; Giester, G. Crystal Structure of $W_{1-x}B_3$ and Phase Equilibria in the Boron-Rich Part of the Systems Mo-Rh-B and W-{Ru,Os,Rh,Ir,Ni,Pd,Pt}-B. *J. Phase Equilibria Diffus.* **2014**, *35*, 384–395. [CrossRef]
25. Haschke, H. Strukturchemische Untersuchungen an Komplexboriden und -Carbiden, Sowie an Siliciden und Germaniden Seltener Metalle. Ph.D. Thesis, Universität Wien, Vienna, Austria, 1967.
26. Rogl, P.; Nowotny, H.; Benesovsky, F. Komplexboride mit ReB2-Struktur. *Monatshefte für Chemie* **1970**, *101*, 27–31. [CrossRef]
27. Brukl, C.E.; Rudy, E. *Ternary Phase Equilibria in Transition Metal—Boron—Carbon—Silicon Systems, Part II: Ternary Systems. Volume XIV The Hafnium—Iridium—Boron—System*; Air Force Materials Laboratory: Wright-Patterson Air Force Base, OH, USA, 1967. Available online: https://apps.dtic.mil/sti/pdfs/AD082649 (accessed on 7 March 2021).
28. Rogl, P.; Nowotny, H. Studies of the (Sc, Zr, Hf)-(Rh, Ir)-B systems. *J. Less Common Met.* **1979**, *67*, 41–50. [CrossRef]
29. Sichevych, O.; Flipo, S.; Ormeci, A.; Bobnar, M.; Akselrud, L.; Prots, Y.; Burkhardt, U.; Gumeniuk, R.; Leithe-Jasper, A.; Grin, Y. Crystal Structure and Physical Properties of the Cage Compound $Hf_2B_{2-2\delta}Ir_{5+\delta}$. *Inorg. Chem.* **2020**, *59*, 14280–14289. [CrossRef] [PubMed]
30. Lozanov, V.V.; Utkin, A.V.; Gavrilova, T.A.; Titov, A.T.; Beskrovny, A.I.; Letyagin, G.A.; Romanenko, G.V.; Baklanova, N.I. New hard ternary Hf–Ir–B borides formed by reaction hafnium diboride with iridium. *J. Am. Ceram. Soc.* **2021**, *105*, 2323–2333. [CrossRef]
31. Hermus, M.; Fokwa, B.P. Zr2Ir6B with an eightfold superstructure of the cubic perovskite-like boride ZrIr3B0.5: Synthesis, crystal structure and bonding analysis. *J. Solid State Chem.* **2010**, *183*, 784–788. [CrossRef]
32. Bannykh, D.A.; Golosov, M.A.; Lozanov, V.V.; Baklanova, N.I. Effect of Mechanical Activation of Iridium on Its Reaction with Refractory Carbides. *Inorg. Mater.* **2021**, *57*, 879–886. [CrossRef]
33. Havinga, E.; Damsma, H.; Hokkeling, P. Compounds and pseudo-binary alloys with the $CuAl_2$(C16)-type structure I. Preparation and X-ray results. *J. Less Common Met.* **1972**, *27*, 169–186. [CrossRef]
34. Kiessling, R.; Wetterholm, A.; Sillén, L.G.; Linnasalmi, A.; Laukkanen, P. The Crystal Structures of Molybdenum and Tungsten Borides. *Acta Chem. Scand.* **1947**, *1*, 893–916. [CrossRef]
35. Kiessling, R.; Hagdahl, L.; Sillén, L.G.; Rottenberg, M. The Borides of Some Transition Elements. *Acta Chem. Scand.* **1950**, *4*, 209–227. [CrossRef]
36. Balagurov, A.M.; Beskrovnyy, A.I.; Zhuravlev, V.V.; Mironova, G.M.; Bobrikov, I.A.; Neov, D.; Sheverev, S.G. Neutron diffract tometer for real-time studies of transient processes at the IBR-2 pulsed reactor. *J. Surf. Investig.* **2016**, *10*, 467–479. [CrossRef]
37. Zeiringer, I.; Cheng, X.; Chen, X.-Q.; Bauer, E.; Giester, G.; Rogl, P.F. Crystal structures and constitution of the binary system iridium-boron. *Sci. China Mater.* **2015**, *58*, 649–668. [CrossRef]
38. Huang, Y.; Wu, B.; Li, F.; Chen, L.; Deng, Z.; Chang, K. First principles and calphad and calphad type study of the Ir-Mo and Ir-W system. *J. Min. Metall. Sect. B Metall.* **2020**, *56*, 109–118. [CrossRef]
39. Okada, S.; Kudou, K.; Lundström, T. Preparations and Some Properties of W2B, δ-WB and WB2 Crystals from High-Temperature Metal Solutions. *Jpn. J. Appl. Phys.* **1995**, *34*, 226–231. [CrossRef]
40. Berlin, J. Analysis of Boron with Energy Dispersive X-ray Spectrometry. *Imaging Microsc.* **2011**, *13*, 19–21. Available online: https://www.yumpu.com/en/document/read/33185105/analysis-of-boron-with-energy-dispersive-x-ray-spectrometry-bruker (accessed on 3 January 2015).
41. Ruiz-Vargas, J.; Siredey-Schwaller, N.; Noyrez, P.; Mathieu, S.; Bocher, P.; Gey, N. Potential and limitations of microanalysis SEM techniques to characterize borides in brazed Ni-based superalloys. *Mater. Charact.* **2014**, *94*, 46–57. [CrossRef]
42. Bearden, J.A. X-ray Wavelengths. *Rev. Mod. Phys.* **1967**, *39*, 78–124. [CrossRef]
43. Toby, B.H.; von Dreele, R.B. *GSAS-II*: The genesis of a modern open-source all purpose crystallography software package. *J. Appl. Crystallogr.* **2013**, *46*, 544–549. [CrossRef]